Flow field and temperature distribution in an atmospheric pressure rotating gliding arc reactor

J. Martin-del-Campo[1], G. Trenchev[2], S. Coulombe[1] and A. Bogaerts[2]

[1]*Plasma Processing Laboratory, Department of Chemical Engineering, McGill University, Montréal, Québec, Canada*
[2]*Research group PLASMANT, Department of Chemistry, University of Antwerp, Antwerp, Belgium*

Abstract: The flow field and temperature distribution along an atmospheric pressure rotating gliding arc reactor were investigated experimentally and through numerical simulations. Argon was injected in the reactor by a 6-point tangential gas injector assembly, thus enabling the arc rotation and upward displacement, and co-driven by a static magnetic field. Simulations were performed with flow rates of 3.7, 4.7 and 6.7 SLPM. The temperature distribution along the axis of the reactor was measured for average power levels of 21.0 and 26.6 W modelling the last one by defining an elongated torus-like shape heat source.

Keywords: rotating gliding arc, warm plasma, flow field, temperature distribution, energy

1. General

Gliding arc discharges have been extensively studied for reforming reactions, pollutant degradation, combustion enhancement, waste and exhaust treatment [1–5] among other applications. They present several advantages compared to other plasma sources. For instance, gliding arc discharges can operate at atmospheric pressure (or higher), the reactor construction is simple, which translates in low cost compared to several currently used reactors, and they operate over a wide range of flow rates and power levels (W to several kW). Besides, gliding arc discharges feature properties characteristic of thermal and non-thermal plasmas [4].

A gliding arc discharge relies on an auto-oscillating periodic phenomenon that develops between two diverging electrodes submerged in a flowing gas [6]. To sustain the gliding arcs, a high-voltage generator (several tens of kVs) produces the electric field required for gas breakdown at the short inter-electrode distance (~30 kV cm^{-1} in atmospheric air), while a second, mid-voltage range (a few kVs) but higher-current capability power supply takes over for arc maintenance [1,7].

Three phases occur during the gliding arc evolution: 1) the thermal stage when the gas breakdown takes places at the narrowest inter-electrode gap, 2) the quasi-equilibrium stage when the arc is then forced to move away from the closest gap area by a gas flow (or natural convection in vertical gliding arc systems). In this phase, the arc length increases, which is associated with a voltage increase, 3) once the arc voltage (arc length) becomes too large for the power supply, the non-equilibrium stage is reached, and the next arc is generated at the lowest inter-electrode gap [1,4,6,7]

As the length of the arc increases, the gas temperature decreases because the heat losses from the plasma column begin to exceed the energy supplied by the source. Therefore, it is not possible to sustain the plasma in thermodynamic equilibrium anymore. Thus, the discharge plasma rapidly cools to the gas temperature, while the electrons maintain a high temperature, T_e ~1 eV (11,600 K) [1,7,8].

To enhance the reaction plasma volume and its uniformity between the electrodes, a special configuration, called a rotating gliding arc (RGA) has been developed by different authors [3,5,9,10]. The RGA uses a tangential injection of the reactant gas to form a swirling flow field in the reactor. As the arc is pushed away from the breakdown area, it swirls and elongates, forming a larger plasma volume [10]. The arc can also be forced to rotate by the action of an external magnetic field (Lorentz force) [5,7,10]. Gas swirl and magnetic forces accelerate the rotation of the arc, increasing the residence time of the reactants as well as the contact area between the reactants and the plasma, thus enhancing the performance of the conventional gliding arc discharge.

The properties of the gliding arc depend on the system parameters such as power input and flow rate [11]. This contribution presents a comparative study of the measured and calculated flow field and temperature distributions along a small-scale RGA operating in atmospheric pressure argon.

2. Experimental setup

The RGA reactor was adapted from [7]. A conical live electrode (cathode) is concentrically-mounted inside of the ground electrode that consists of a hollow anode cylinder (Fig. 1). Both electrodes are made of stainless steel 316 with the shortest gap between them of 2.16 mm. Downstream, this inter-electrode gap increases up to 8.76 mm. The length of the cone-shaped cathode is 30.48 mm, with minimum and maximum diameters of 1.52 mm and 14.73 mm, respectively, and an angle of 12.2°. The ground electrode has an inner diameter of 19.05 mm and a total length of 482.6 mm. The reactor is terminated with CF components, enabling gas exhaust on the side port and direct line of sight view along the reactor axis. An isolating jacket was provided to the reactor to avoid heat losses through the walls of the reactor. Argon (99.998 % purity) is injected tangentially through the reactor by six gas injectors mounted at an angle of 20º axially and 30° radially. The live electrode is powered by a homemade dual-stage pulsed DC power supply, consisting of a high-voltage arc igniter and a low current driver power supply. A stack of ring magnets mounted around the anode cylinder adds a static axial magnetic field, which resulting Lorentz force acts along the gas drag force [9]. The arc and gas flow are set into an anticlockwise swirl.

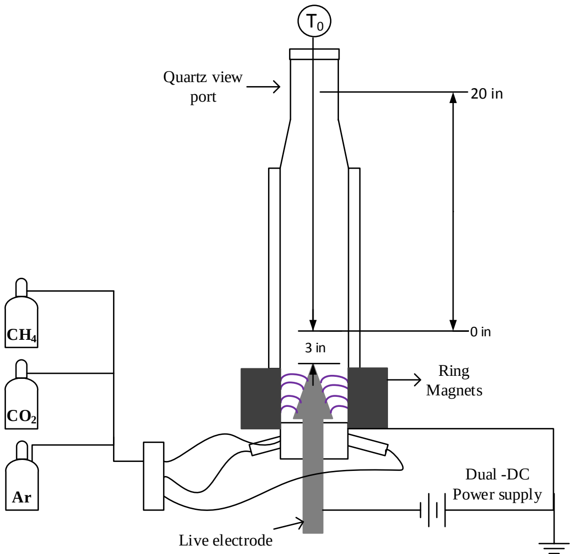

Fig. 1 Schematic of the RGA reactor setup.

The voltage, *V(t)*, and current, *I(t)*, of the RGA are monitored using a high-voltage probe (B&K Precision PR55) and a passive voltage probe (Tektronix P2200) across a 1 Ω shunt resistor, connected to a digital oscilloscope (PicoScope 2207B). Two different experimental conditions were set by changing the internal resistance of the current driver power supply (1075 and 535 Ω), for two input voltages (V_C) of -266 and -252 V, respectively. Argon was injected in the reactor at a flow rate of 3.7 SLPM. Figure 2 shows typical voltage and current waveforms measured, as well as the instantaneous calculated power for V_C=-252 V. The reactor was operated for 180 minutes and steady state was achieved after ~140 minutes (Fig. 4). The gas temperature was measured with a type K thermocouple located 3 in. (76.2 mm) above the tip of the cathode cone. By moving the thermocouple along the reactor, after steady state was achieved, a temperature profile along the reactor axis was obtained (Fig. 5). Note that in Figure 1, the z=0 position corresponds to 3 in. (76.2 mm) above the cathode tip (indicated in Fig. 1), and the measurements were obtained every inch (25.4 mm) from this point, going all the way to the end of the reactor.

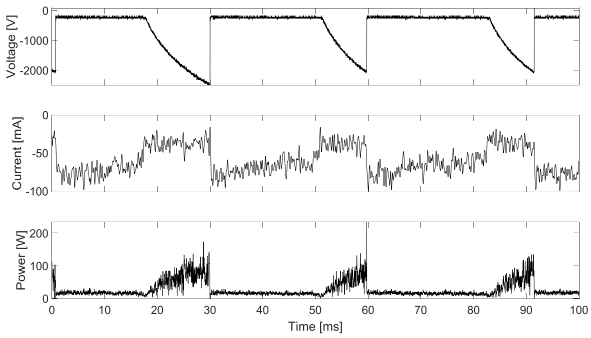

Fig. 2. Discharge voltage, current and instantaneous power signals for V_C = -252 V

To determine the behaviour of the gas inside the reactor, flow simulations were carried out using Comsol Multiphysics 5.4 for flow rates of 3.7, 4.7 and 6.7 SLPM. The thermodynamic properties of Argon were also pre-defined in Comsol. The Navier-Stokes equations were solved using a RANS turbulent model (k-epsilon). The turbulent heat conductivity in the reactor was estimated using the Kays-Crawford model. The following equations were solved for the gas flow in the 3D model:

$$\nabla.\left(\rho\overrightarrow{u_g}\right) = 0 \tag{1}$$

$$\rho(\overrightarrow{u_g}.\nabla)\overrightarrow{u_g} = \nabla.\left[-p\vec{I} + (\mu+\mu_T)\left(\nabla\overrightarrow{u_g} + \nabla\left(\overrightarrow{u_g}\right)^T\right) - \frac{2}{3}(\mu+\mu_T)(\nabla.\overrightarrow{u_g})\vec{I} - \frac{2}{3}\rho s_T\vec{I}\right] + \vec{F} \tag{2}$$

Equations 1 and 2 represent the mass and momentum continuity equations in the RANS model, where ρ stands for the gas density, $\overrightarrow{u_g}$ is the gas flow velocity vector, superscript T stands for transposition, p is the gas pressure, μ is the dynamic viscosity of the fluid, μ_T is the turbulent viscosity of the fluid, s_T is the turbulent kinetic energy, $\vec{I}$ is the unity tensor and $\vec{F}$ is the body force vector.

The energy equation is:

$$\rho C_p\frac{\partial T_g}{\partial t} + \rho C_p\overrightarrow{u_g}\cdot\nabla T_g - \nabla\cdot\left((k_g+k_T)\nabla T_g\right) = Q \tag{3}$$

where C_p is the specific heat capacity of the gas, k_g is the temperature-dependent gas thermal conductivity (based on a material look-up table), k_T is the turbulent heat conductivity of the fluid, T_g is the gas temperature and Q accounts for the artificial heat source representing the plasma.

3. Results

The evolution of the amount of energy deposited in the RGA up to time *t*, *E(t)*, was determined using the following equation:

$$E(t) = \int_0^t V(t)\ I(t)dt \tag{4}$$

Figure 3 shows the energy evolution for 25 s for the two conditions, V_C= -266 and -252 V. By determining the slope of the energy line, average powers of 21.00 ± 0.31 W and 26.60 ± 0.76 W were obtained, respectively.

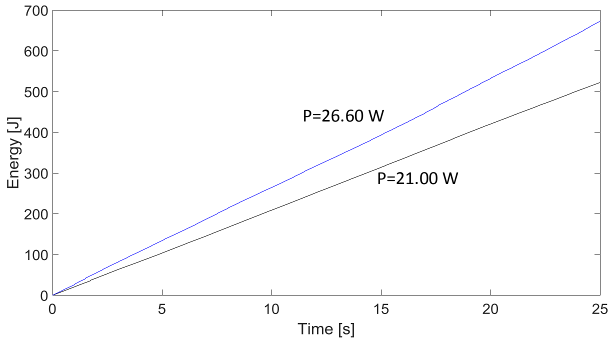

Figure 3. Temporal evolution of the accumulated deposited energy evolution for the RGA discharge for V_C=-252 (blue curve) and -266 V (black curve).

The effect of RGA power on the measured gas temperature distribution is reported in Fig. 4. The overall temperature increase, $\Delta T = T_{final} - T_{initial}$, for the power levels of 21.00 and 26.60 W was 21 and 23 °C, respectively.

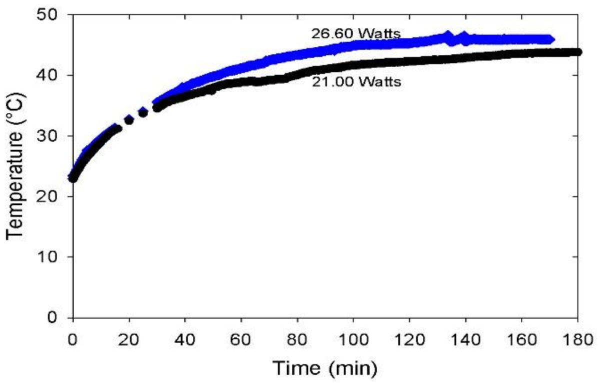

Fig. 4. Temporal evolution of gas temperature at z=0 mm for the two power levels and a total argon flow rate of 3.7 SLPM.

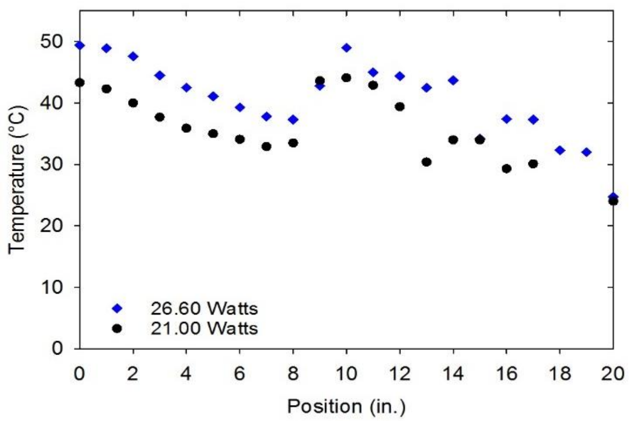

Fig. 5. Temperature profile along the reactor for power levels of 21.00 and 26.60 W for a total argon flow rate of 3.7 SLPM.

Figure 5 reports the temperature profile of the gas along the reactor. As expected, when the gas is further from the plasma source, the temperature decreases lineally, however, from position 9 to 13 in. (middle of the reactor) there is an increase of temperature, having the maximum temperature at position 10 in. and decreasing afterwards.

To determine the total power deposition, a heat source is defined as an elongated torus-like shape surrounding the cathode (Fig. 6). Integrating the magnitude of this defined profile in the reactor volume yields 26.60 W of total power deposition, which corresponds to the average value obtained from the experimental results for V_C=-252 V.

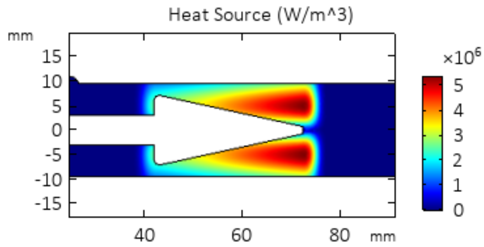

Fig. 6. Cathode heat source shape in the reactor

Figure 7 shows the gas flow vector for flow rates of 3.7, 4.7 and 6.7 SLPM. Note that the radial flow velocity is more significant with higher flow rates. At 3.7 SLPM, the flow vortex is almost non-present above the cathode, while at 6.7 SLPM, the vortex can be clearly observed. This would naturally affect the turbulence development and, in addition to the increased convective heat transfer, the turbulent heat flux in the gas will also be higher. In Figure 8, the effective thermal conductivity (i.e. gas conductivity + turbulent enhancement) is plotted in 2D projections across the reactor centre, for the 3 different flow rates. A turbulent enhancement zone can be clearly seen at 6.7 SLPM.

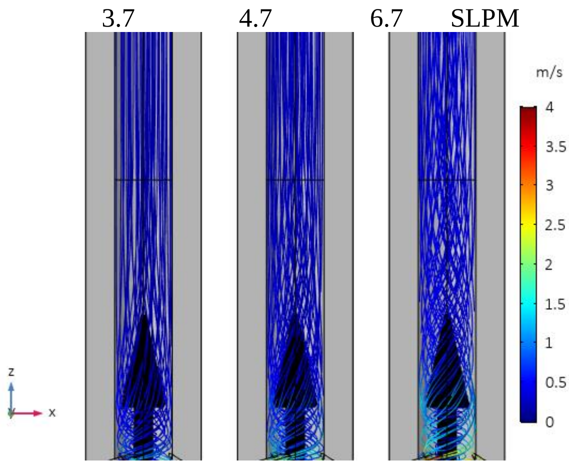

Fig. 7. Gas flow vector (streamlines) for 3.7, 4.7 and 6.7 SLPM, respectively.

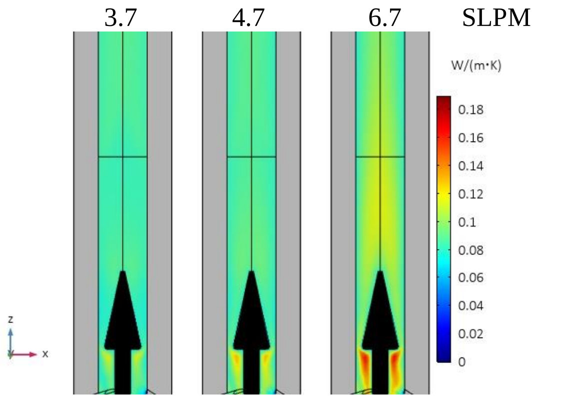

Fig. 8. Effective thermal conductivity for different flow rates.

The calculated temperature profiles are presented in Figure 9. Note that this is the resulting gas temperature from a stationary solution of the heat equation, and the heat losses toward the walls were not included (the walls are adiabatic).

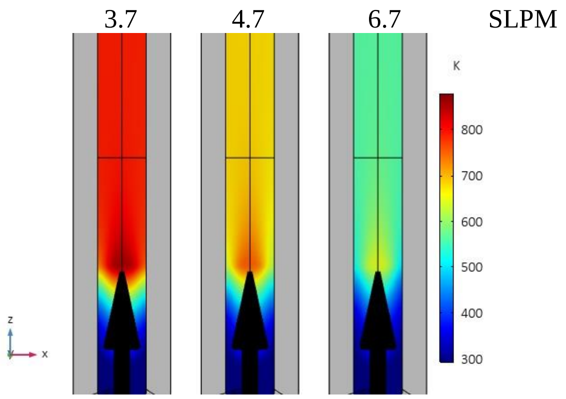

Fig. 9. Calculated temperature profiles for different argon flow rates and 26.60 W of power deposition.

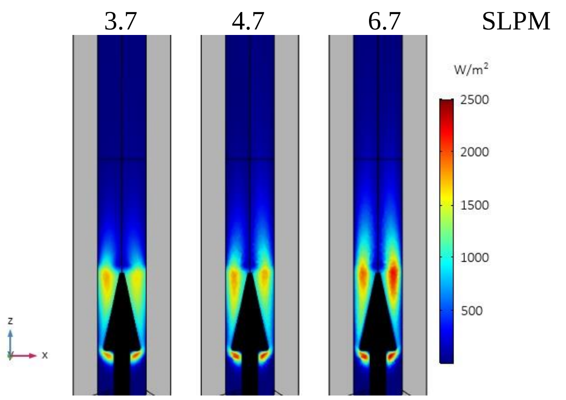

Fig. 10. Calculated turbulent heat flux magnitude for different argon flow rates and 26.60 W of power deposition.

As shown in Figure 10, there is about 50% of turbulent heat conductivity enhancement between the minimum (3.7 SLPM) and maximum (6.7 SLPM) flow rate. This is reflected in the resulting temperature in the reactor (Fig. 8).

4. Conclusions and future work

The temperature distribution along an atmospheric pressure rotating gliding arc reactor were investigated experimentally and through numerical simulations. By measuring the electrical characteristics of the gliding arc discharge, average power levels of 21.00 and 26.60 W were determined for the two experimental conditions. The average power level of 26.60 W was simulated in the reactor by defining an elongated torus-like shape heat source. The gas temperature distribution along the reactor axis was also determined.

On the modelling side, flow simulations were carried out for flow rates of 3.7, 4.7 and 6.7 SLPM and an average power of 26.60 W. The flow vector was obtained, and compared for the different flow rates, showing a more significant vortex development at higher flow rates. The overall flow velocity is low, indicating the main arc rotation comes from the Lorentz force produced by the ring magnets.

The turbulent heat conductivity is also obtained using the Kays-Crawford model for turbulent flows. A minor turbulent heat flux is observed at low flow rates, with a more significant enhancement at 6.7 SLPM, meaning that low flow rates do not provide significant turbulent dissipation.

To gain full comparison with the temperatures measured experimentally, the heat losses towards the wall, as well as the heat transfer towards the thermocouple probe have to be modelled as well.

5. References

[1] A. Fridman, S. Nester, L.A. Kennedy, A. Saveliev, O. Mutaf-Yardimci, Prog. Energy Combust. Sci. 25 (1999) 211–231.

[2] E. Cleiren, S. Heijkers, M. Ramakers, A. Bogaerts, ChemSusChem 10 (2017) 4025–4036.

[3] M. Ramakers, G. Trenchev, S. Heijkers, W. Wang, A. Bogaerts, ChemSusChem 10 (2017) 2642–2652.

[4] X. Tu, J.C. Whitehead, Int. J. Hydrogen Energy 39 (2014) 9658–9669.

[5] A. Fridman, A. Gutsol, S. Gangoli, Y. Ju, T. Ombrello, J. Propuls. Power 24 (2008) 1216–1227.

[6] L.A. Fridman, A.Kennedy, Plasma Physics and Engineering, Taylos & Francis, United States of America, 2004.

[7] M. McNall, S. Coulombe, J. Appl. Phys. 51 (2018).

[8] H. Lee, H. Sekiguchi, J. Phys. D. Appl. Phys. 44 (2011) 274008.

[9] N. Hwang, J. Lee, D.H. Lee, Y.-H. Song, Plasma Chem. Plasma Process. 32 (2012) 187–200.

[10] H. Zhang, X.D. Li, Y.Q. Zhang, T. Chen, J.H. Yan, C.M. Du, IEEE Trans. Plasma Sci. 40 (2012) 3493–3498.

[11] H. Zhang, F. Zhu, X. Tu, Z. Bo, K. Cen, X. Li, Plasma Sci. Technol. Plasma Sci. Technol. 18 (2016) 473–477.